Research Square

Preprints are preliminary reports that have not undergone peer review.
They should not be considered conclusive, used to inform clinical practice,
or referenced by the media as validated information.

Hydrogen blending amplifies seismic risk to global gas pipelines

Y. Cheng

fcheng@ucalgary.ca

University of Calgary https://orcid.org/0000-0002-3379-1828

Jinkun Men

Ningbo Institute of Materials Technology and Engineering

Hongfang Lu

Ningbo Institute of Materials Technology and Engineering, Chinese Academy of Sciences
https://orcid.org/0000-0002-5172-9008

Yinghao Sun

University of Toronto

Jie Zhang

Southwest Petroleum University

Article

Keywords:

Posted Date: November 3rd, 2026

DOI: https://doi.org/10.21203/rs.3.rs-11324496/v1

License: This work is licensed under a Creative Commons Attribution 4.0 International License.
Read Full License

Additional Declarations: There is **NO** Competing Interest.

Hydrogen blending amplifies seismic risk to global gas pipelines

Jinkun Men[a,b], Hongfang Lu[a], Yinghao Sun[c], Jie Zhang[b], Y. Frank Cheng[a,d*]

[a] State Key Laboratory of Advanced Marine Materials, Ningbo Institute of Materials Technology and Engineering, Chinese Academy of Sciences, Ningbo, China

[b] Key Laboratory of Oil & Gas Equipment of the Ministry of Education, Southwest Petroleum University, Chengdu, China

[c] Department of Materials Science and Engineering, University of Toronto, Toronto, ON, Canada

[d] Department of Mechanical Engineering, University of Calgary, Calgary, AB, Canada

*Corresponding author: Y. Frank Cheng, E-mail: fcheng@ucalgary.ca

Abstract

Repurposing existing natural gas pipelines for hydrogen service provides a promising approach for accelerated development of hydrogen economy. Yet hydrogen blending remains an underestimated amplifier of seismic risk to the pipelines. Herein, we assess the seismic hazard exposure, failure risk, and resilience loss on 2,554 operating pipelines, including 1,731 fault-crossing risk points and 476 topological systems, in the world. Results demonstrate that a prolonged hydrogen exposure elevates failure risk of the pipelines, with the failure probability increasing by nearly 40 times at certain sensitive crossings. The risk amplification is primarily driven by accumulated hydrogen damage to the pipelines, rather than by extreme seismic hotspots. Generally, the resilience loss of pipelines is topology-dependent, with main trunklines most affected. The findings exhibit a cross-scale risk spanning from pipe material degradation and structural failure to infrastructure disruption. It is proposed that evaluating the existing pipelines for hydrogen transport must include the seismic risk.

Hydrogen will be a critical player in energy transition owing to its high gravimetric energy density and compatibility with renewable energy and electricity[1,2,3]. To date, more than 100 countries have developed their national hydrogen strategies. The hydrogen deployment at scale can potentially contribute up to 20% towards a net-zero economy[4,5,6]. Scaling the hydrogen economy requires extensive infrastructure for production, storage, and transport[7,8,9]. The International Energy Agency reported that around 40,000 km of pipelines will be built for hydrogen transport by 2035[10]. Particularly, the majority of them will come from repurposing roughly 1.45 million km of existing natural gas pipelines[10,11,12].

Blending hydrogen into existing pipelines is regarded as an effective strategy for large-scale hydrogen transport[1,13,14]. In 2023, the UK government proposed to support blending up to 20%(v/v) hydrogen into Great Britain gas distribution networks[15]. The HyDeploy project reported that hydrogen could be safely blended into a natural-gas distribution network at concentrations of up to 20% without modifications to end-use gas appliances[16]. In France, the GRHYD project progressively increased hydrogen blending from 6% to 20% in a local distribution grid[17]. The Jupiter 1000 project further proposed industrial-scale Power-to-Gas injection into the transmission network[18]. Nowadays, hydrogen blending in natural gas transmission pipelines for large-scale and long-distance transportation is limited. Most operating projects are confined to local distribution networks and trial demonstrations.

Natural gas pipelines were designed and operated for methane service, rather than for pure hydrogen or hydrogen-containing gas mixtures. From the material compatibility perspective, hydrogen gas molecules (H_2) can absorb on steel surface and dissociate into hydrogen atoms (H) under pipeline operating conditions[19]. H atoms can penetrate into the steel subsurface, diffuse within iron lattice, and can become accumulated at microstructural traps such as grain boundaries, dislocations and secondary phase particles. The mechanical properties of the steel can be degraded by H effect. Sometimes, cracks are initiated with the assistance of stress concentration[19,20,21]. In

addition to the H effect on material performance, the hydrogen gas leakage and combustion safety, end-use operability and regulatory blending limits should also be considered in the blending projects[19,20,22].

Hydrogen-induced material degradation is typically a delayed and time-cumulative process, developing over weeks, months, or even years[13,19]. During operation, pipelines experience threats by external loading, such as seismic fault displacement[23,24]. The coupling effect between long-term hydrogen exposure and extreme seismic loading may challenge the applicability of existing pipeline seismic design and technical standards, which were developed without considering the hydrogen effect on material properties[11,25]. Relevant studies have been conducted in assessment of the hydrogen effect[26,27], pipeline seismic failure modelling [28,29] and system resilience analysis[30,31]. However, the synergism between hydrogen and seismic effects may lead to overestimation of the pipeline safety in hydrogen service by the existing standards and codes.

This study attempts to understand how hydrogen blending may reshape seismic threats to natural gas pipeline infrastructure worldwide. Herein, we compile data on spatially explicit natural gas transmission pipelines from the Global Gas Infrastructure Tracker with the database of global seismic hazards and active faults from the Global Earthquake Model, determining the exposure of 2,554 operating natural gas pipelines to seismic hazard, identifying 1,745 fault-crossing risk points. We then estimate annual seismic failure probabilities at 1,731 validated fault-crossing risk points across 476 pipelines with various hydrogen blending ratios (i.e., 5%, 10%, 15% and 20%) and exposure times (i.e., 10, 20 and 30 years), which are represented as weighted multigraphs to evaluate the effect of isolated and common-fault multi-point failures on seismic resilience of the pipelines. Our findings suggest that a cross-scale program must be urgently developed to assess the hydrogen effect on degradation of material properties, increased seismic risk and resilience loss of pipelines when repurposed for hydrogen service.

Results

Highly non-uniform exposures of global natural gas pipelines to seismic hazard

The seismic hazard exposures are assessed across 2,554 operating natural gas pipelines with a total length of approximately 1.11 million km in the world. The asset-level gas transmission pipeline data from the Global Gas Infrastructure Tracker, the global earthquake model (GEM) global seismic hazard map (version 2023.1), and the GEM global active faults database are combined to develop a global map illustrating the geographic distribution of peak ground acceleration (PGA) and active fault traces on operating natural gas pipelines, as shown in **Fig. 1a**. Using the 95th percentile of PGA sampled along each pipeline, five seismic hazard exposure levels (SHELs) are established, as seen in **Fig. 1b**. Notably, 621 pipelines of 246,651 km in length are assigned to SHEL 4 or 5. Obviously, the seismic hazard exposure of pipelines is highly non-uniform. As indicated in **Fig. 1c** and Extended Data Table 1, the United States owns the largest infrastructure scale, followed by China and Russia. More than 10,000 km of pipelines in the United States and over 9,000 km in China are exposed to SHEL 5. Countries located near major seismic belts, such as Türkiye, Iran, Pakistan and Greece on the Alpide belt, and Mexico, Chile, Japan and New Zealand around the circum-Pacific seismic belt, show extremely great proportions of high-exposure-level pipelines[16, 2]. Further, 1,745 pipeline-fault intersections are identified as specific fault-crossing risk points, more than half of which are located in the United States, China, Türkiye, Iran and Italy (**Fig. 1d** and Extended Data Table 2). There are 65.7% of risk points exposed to SHEL 4 or 5, as seen in **Fig. 1e**. The results tell that the pipeline network as a whole shifts towards exposure to higher seismic hazards (**Fig. 1f**).

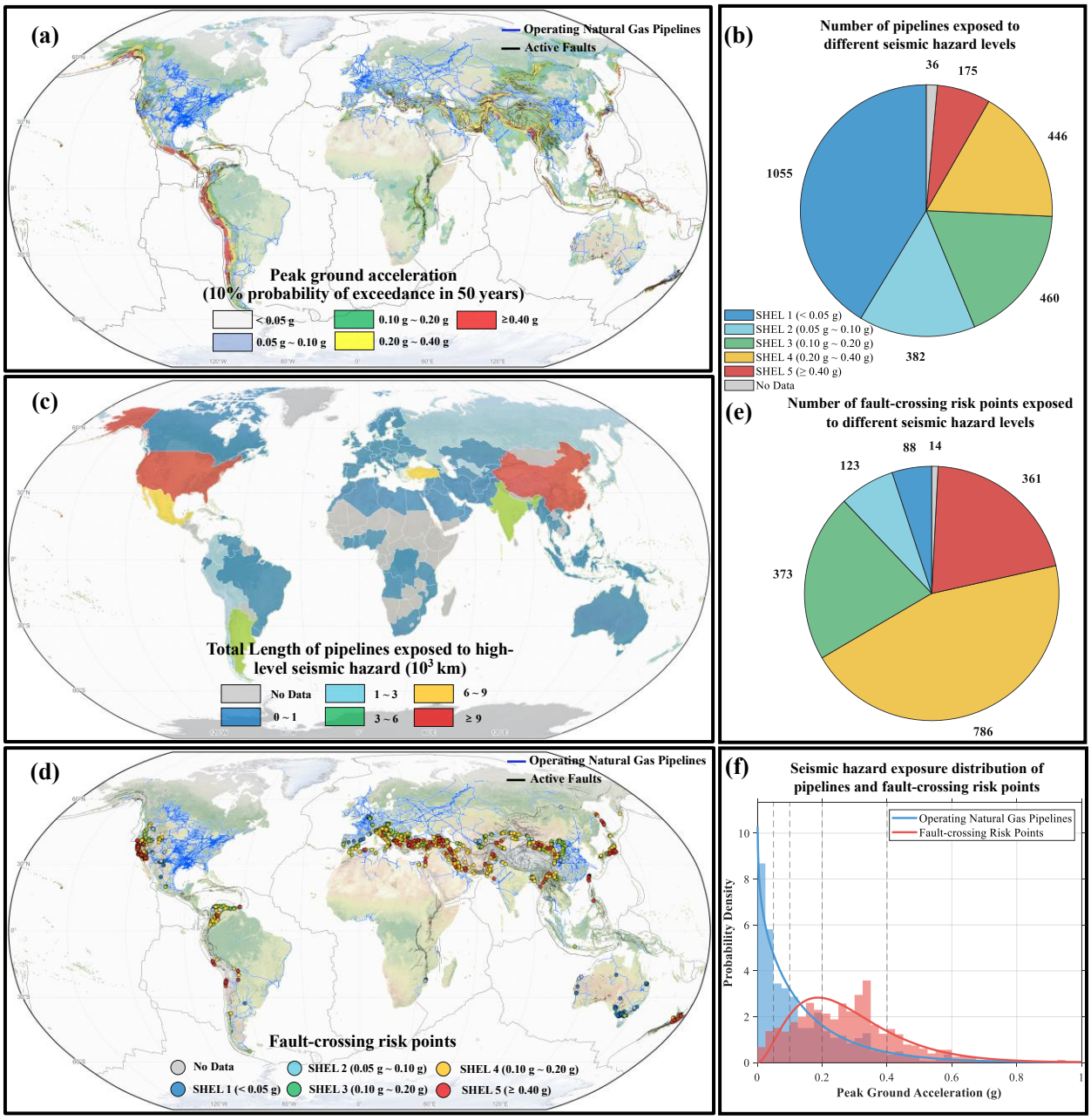


Fig. 1. Analyses of seismic hazard exposures of operating natural gas pipelines worldwide. **a.** Global map of 2,554 operating natural gas pipelines, peak ground acceleration (PGA), and 13,696 active fault traces. The natural gas pipelines are shown as blue polylines, and active faults as black traces. The PGA layer is from the global seismic hazard map, and represents PGA on reference rock conditions with a 10% probability of exceedance in 50 years. **b.** Number of pipelines exposed to different seismic hazard levels. **c.** National distribution of the length of operating natural gas pipelines exposed to SHEL 5. **d.** Identification of fault-crossing risk points. **e.** Number of fault-crossing risk points exposed to different seismic hazard levels. **f.** Distribution of seismic hazard exposure of pipelines and fault-crossing risk points.

Seismic failure risk at pipeline-fault crossings enhanced by hydrogen effect

The annualized pipeline failure probabilities ($P_{an,f}$) caused by potential seismic fault displacement at 1,731 valid fault-crossing risk points are calculated, and the results are shown in **Figs. 2a, b and c**, as well as Extended Data Table 3. Each data point represents 500 Monte Carlo realizations, yielding 865,500 failure probability estimates for combined hydrogen blending ratio and exposure time scenarios. At specific exposure times, when the hydrogen blending ratio is increased from 5% to 20%, the distribution of $P_{an,f}$ is shifted towards greater values. The arithmetic mean, $\mu(P_{an,f})$, the 50th percentile of annualized pipeline failure probability, $P_{50}(P_{an,f})$, and the 95th percentile of annualized pipeline failure probability, $P_{95}(P_{an,f})$, increase by 113.5~167.0%, 265.0~360.4% and 88.0~95.6%, respectively. The resulting histograms become broader, right-skewed and multimodal, consistent with a substantial heterogeneity among global fault-crossing risk points and seismic hazard exposures. A small fraction of high-risk realizations contributes disproportionately to the upper tail of the global risk distribution. Accordingly, the markedly increase in $P_{50}(P_{an,f})$, as compared to $P_{95}(P_{an,f})$, indicates that hydrogen blending shifts the seismic risk from local regions towards a broad distribution over the global population of fault-crossing risk points.

Taking the exposure time of 10 years as an example, the time-dependent seismic risk amplification factors, $R_{i,\alpha}^{10\to t}$, for each risk point, i, are calculated, and the results are shown in **Figs. 2d and e**, and Extended Data Table 4. As the hydrogen exposure time increases from 10, 20 to 30 yrs, $GM(R_{i,\alpha}^{10\to t})$, $P_{50}(R_{i,\alpha}^{10\to t})$, $P_{95}(R_{i,\alpha}^{10\to t})$ and $Max(R_{i,\alpha}^{10\to t})$ exceed unity, indicating a persistent increase in the upper-tail annualized seismic failure probability. After 30 years of exposure, an increase of the blending ratio from 5% to 20% raises $P_{95}(R_{i,\alpha}^{10\to 30})$ by 94.2%. $Max(R_{i,\alpha=15\%}^{10\to 30})$ and $Max(R_{i,\alpha=20\%}^{10\to 30})$ reach 10.042 and 11.990, respectively, showing that the prolonged hydrogen exposure extends the upper tail of the risk distribution at a small subset of sensitive crossings.

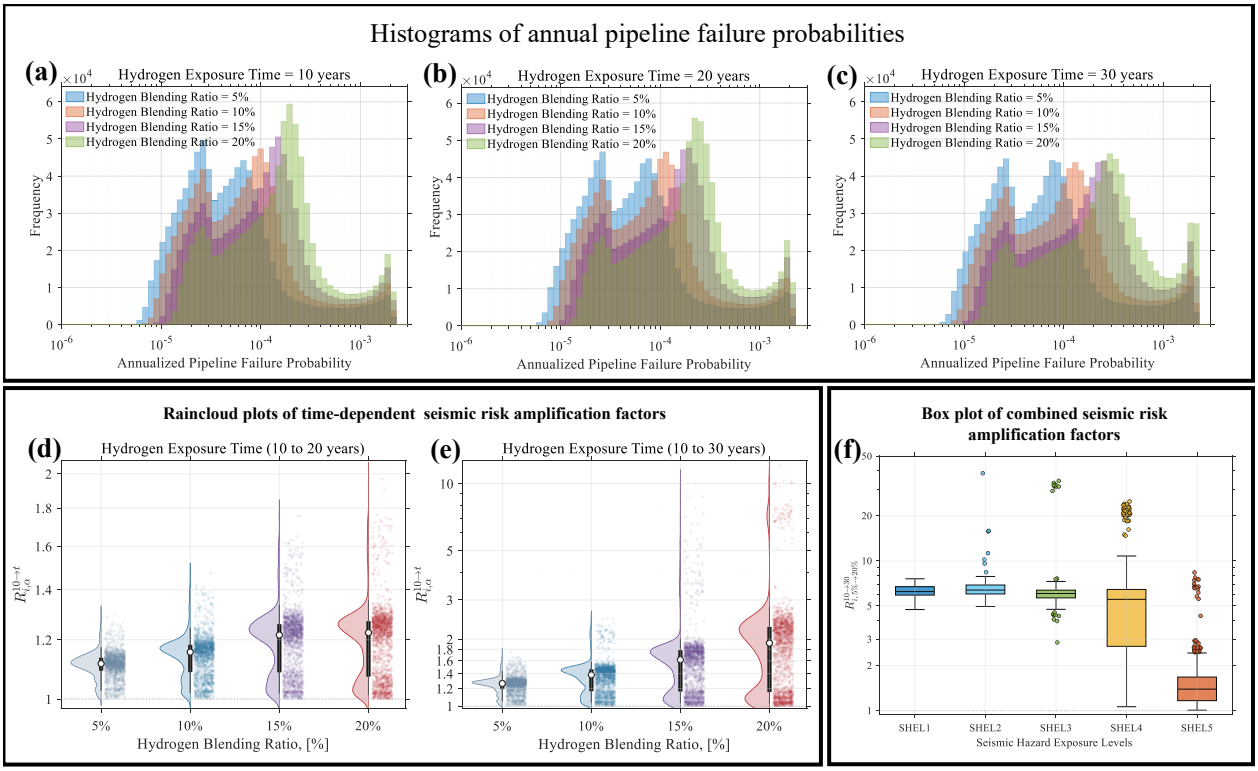


Fig. 2. Analysis results of the annualized pipeline failure probability. **(a, b, c)** Histograms of the annual pipeline failure probability with the exposure times of 10 years, 20 years, and 30 years, respectively. **(d, e)** Raincloud plots of the time-dependent risk amplification factors. **(f)** Box plot of combined seismic risk amplification factors.

Further, take α=5%, t=10 yrs as the reference, the combined seismic risk amplification factors $R^{10\to30}_{i,\,5\%\to20\%}$ is calculated across fault-crossing risk points exposed to specific seismic hazard levels, as seen in **Fig. 2f** and Extended Data Table 5. $R^{10\to30}_{i,\,5\%\to20\%}$ varies non-monotonically over the five SHELs. The risk points exposed to SHEL 4 show the most widespread amplification, with the $P_{95}(R^{10\to30}_{i,5\%\to20\%})$ of 20.671. However, SHELs 2 and 3 produce the greatest $\mathrm{Max}(R^{10\to30}_{i,5\%\to20\%})$ of 38.476 and 34.174, respectively, indicating localized extreme hotspots. The hydrogen-induced seismic risk amplification remains modest under extreme seismic exposure conditions, with $P_{50}\left(R^{10\to30}_{i,5\%\to20\%}\right), i \in \text{SHEL 5}$ of 1.393 and $P_{95}\left(R^{10\to30}_{i,5\%\to20\%}\right), i \in \text{SHEL 5}$ of 2.923. Regardless of whether hydrogen is blended in the pipelines, some risk points exposed to SHEL 5 are already exposed to an extremely high seismic risk.

Global seismic risk landscape of pipelines shaped by long-term hydrogen exposure

The global seismic risk landscape of pipelines is characterized using the 95th percentile of annualized failure probability across all valid fault-crossing points within each country. To reduce the variability caused by limited number of samples, the analysis includes more than five valid risk points across 40 countries. Under the reference scenario of 5% hydrogen blending with 10 years of exposure, the national risk levels vary by nearly 26-fold, with the annualized failure probability from 7.633E-05 (i.e., 0.007633%) in France to 1.981E-03 (i.e., 0.1981%) in Chile, as seen in **Fig. 3a** and Extended Data Table 6, where α is hydrogen blending ratio, t is exposure time, and N_r is the number of valid fault-crossing risk points. Regions with higher values are located around the major seismic belts, including Chile, Peru and Bolivia at the Andes, and Japan and Pakistan around the circum-Pacific and Alpide belts. Only eight countries exceed 0.1%, indicating that the global seismic risk landscape is dominated by a limited number of geographically concentrated hotspots.

Elevated hydrogen blending ratio substantially expands the geographic region with an increased failure risk at specific exposure periods. Take t = 10 yrs of exposure as an example, when the hydrogen blending ratio increases from 5% to 20%, the number of countries with the annualized failure probability exceeding 1.000E-03 (i.e., 0.1%) increases from 8 to 21, with 10 countries exceeding 1.500E-03 (i.e. 0.15%), as shown in **Fig. 3b** and Extended Data Table 7. Countries with a high baseline risk, including Chile, Peru and Japan, show modest increases as the failure probabilities of these countries already approach the upper end of the distribution. A strong increase is observed in countries with a moderate baseline risk. The national $P_{95}(P_{an,f}^{i,(\alpha = 20\%,\ t = 10\ yrs)})$ becomes more than doubled in China and Türkiye, and more than tripled in Iran and Italy, showing that hydrogen blending remarkably elevates the pipeline seismic risk in countries that are conventionally identified as seismic hotspots.

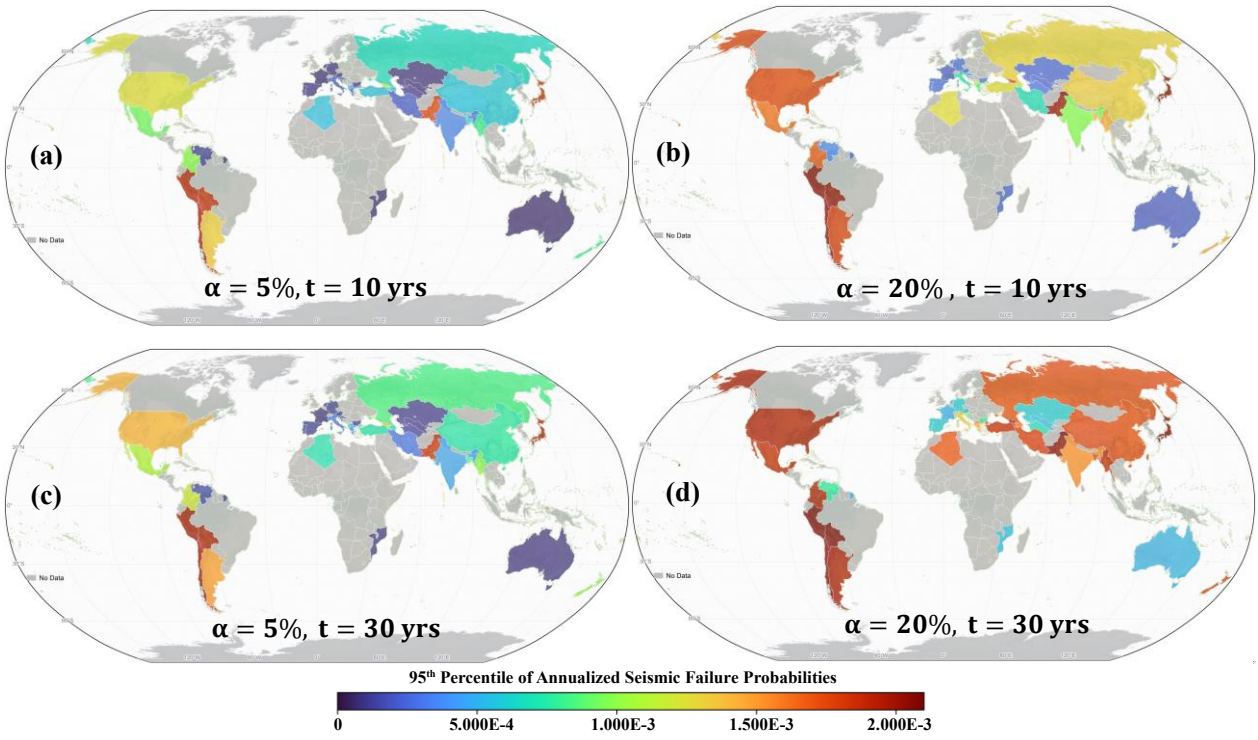


Fig. 3. Global seismic risk landscape characterized by the 95th percentile of annualized failure probability. **a.** 5% hydrogen blending and 10 years of exposure. **b.** 20% hydrogen blending and 10 years of exposure. **c.** 5% hydrogen blending and 30 years of exposure. **d.** 20% hydrogen blending and 30 years of exposure.

A prolonged exposure to hydrogen increases the annualized failure probability, particularly at great blending ratios. For 5% hydrogen blending, an extended exposure from 10 to 30 years increases the number of countries with the annualized failure probability over 0.1% (i.e., 1.000E-03) moderately from 8 to 10, as seen in **Fig. 3c** and Extended Data Table 8. However, the effect becomes more obviously with 20% of hydrogen blending, i.e., after 30 years of exposure, 26 countries exceed 0.1% and 23 exceed 0.15% (**Fig. 3d** and Extended Data Table 9). $P_{95}(P_{an,f}^{i,(\alpha = 20\%,\ t = 30\ yrs)})$ increases from 0.05711% (i.e., 5.711E-04) to 0.1749% (i.e., 1.749E-03) in China, from 0.05475% (i.e., 5.475 E-04) to 0.1875% (1.875E-03) in Türkiye, and from 0.02186% (2.186E-04) to 0.1793% (1.793E-03) in Iran. The median of the annualized failure probability over 40 countries increases by 243%, while the ratio between the highest and lowest values decreases from approximately 26 to 4.2. This convergence does not imply an equal risk, but a transition from

concentrated risk hotspots towards a broadly elevated failure probability across global pipeline infrastructure.

Resilience loss of failed pipelines governed by topological structure

For the 476 pipelines with validated fault-crossing risk points, the spatial geometry of each pipeline is converted into a weighted, undirected multigraph. Pipeline terminals, stations and intermediate segmentation points are represented as nodes, while the physical pipe segments are represented as length-weighted edges. Logical failure connectors are introduced at fault-crossing risk points. The seismic failure of pipelines at a fault-crossing risk point is represented by removal of the corresponding logical failure connector. The resulting topological models contain 16,837 nodes, 40,974 physical edges, and 1,728 logical failure connectors, as shown in Extended Data Table 10. The number of connectors reflects three pairs of spatially coincident risk points associated with various faults. Linear trunklines comprise 409 systems and 125,785 km of pipelines, whereas 44 branched networks account for 48,128 km. By contrast, meshed networks are rare and contain 23 systems only, but extend 111,593 km with 71.4% of nodes and 91.4% of physical edges. Thus, the fault-crossing pipeline infrastructure is dominated by linear systems, while a small number of regional and national pipeline networks reflect the topological complexity.

To link the point-level seismic failure risk with system-level resilience loss, the seismic resilience is characterized with two complementary components, i.e., resistance capacity and absorptive capacity. The resistance capacity describes the ability of pipelines to withstand seismic loading without failures, whereas the absorptive capacity defines the extent to which a pipeline retains connectivity following failure at fault-crossing risk points. The connectivity refers to the extent to which nodes in a pipeline network remain mutually reachable through intact pipeline paths.

It is assumed that the seismic failure at each fault-crossing risk point is regarded as an

independent event. **Figs. 4a, b and c**, and Extended Data Table 11 show the absorptive capacity phase spaces for linear trunklines, branched network, and meshed network, respectively, where the horizontal axis represents retained terminal-to-terminal connectivity (A_T), and the vertical axis represents retained physical connectivity, i.e., $A_P = (A_L + A_{LCC})/2$, where A_L and A_{LCC} are the retained length-weighted network integrity and the largest component size, respectively.

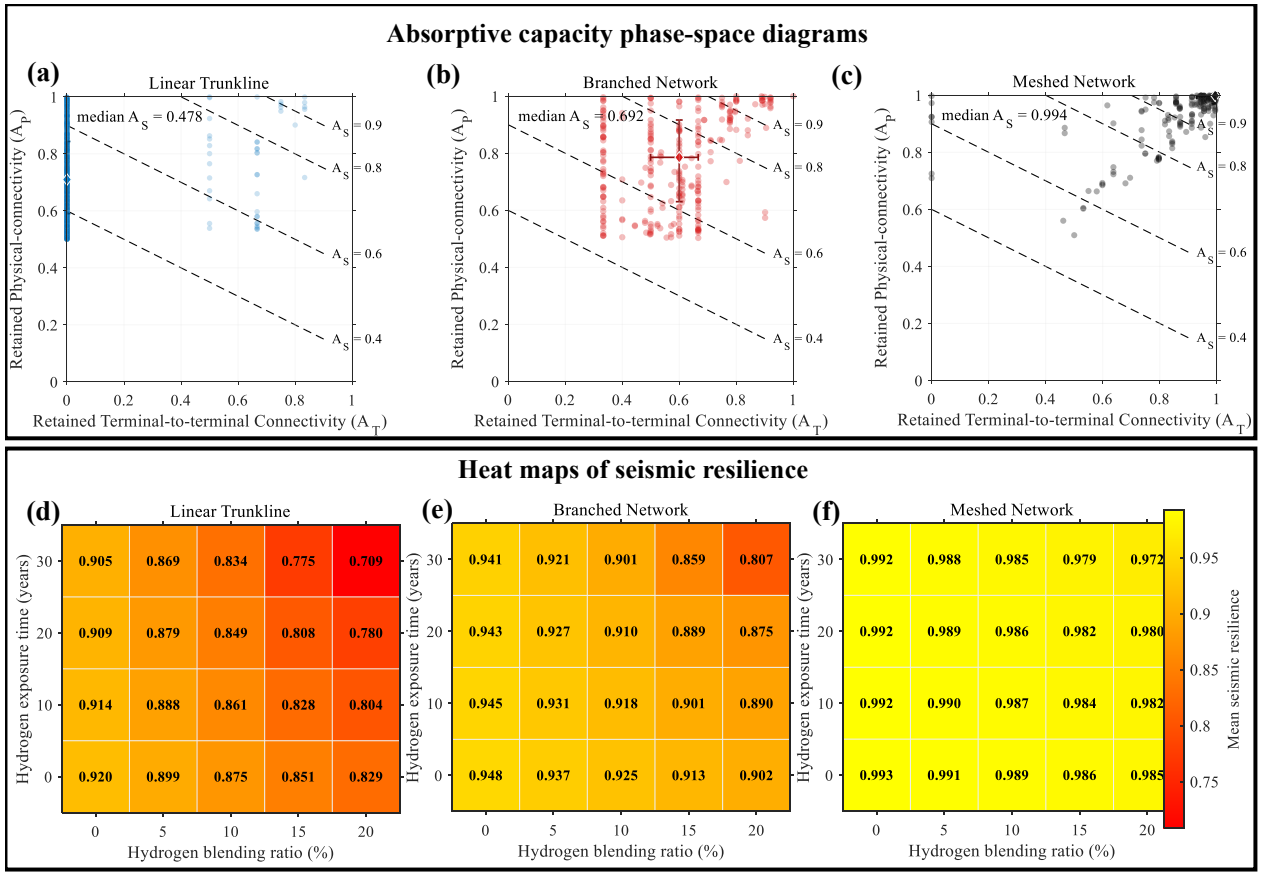


Fig. 4. Seismic resilience analysis of isolated logical failure connector. **(a, b, c)** Absorptive capacity phase-space diagrams, **(d, e, f)** Heat maps of seismic resilience, where mean values of the seismic resilience $SR_{j,i}$ over hydrogen blending ratios and hydrogen exposure times for linear trunklines, branched networks and meshed networks, respectively.

Each point represents one connector-failure case. Black dashed lines refer to equal values of the normalized absorptive capacity metric (A_S), where the states at the upper-right corner indicate a stronger retention of both functional and physical connectivity. The broad dispersion of failure states indicates a pronounced location dependence. Diamonds mean the coordinate-wise medians,

whereas horizontal and vertical bars denote the interquartile ranges of A_T and A_P, respectively. It is seen that the linear trunklines exhibit the lowest absorptive capacity as every connector is a bridge. Accordingly, $\mu(A_T)$ is 0.026 only although $\mu(A_L)$ and $\mu(A_{LCC})$ remain at 0.681 and 0.762, respectively. Branched networks are also bridge-dominated, with 99.6% of connectors are classified as bridges, but occupy a broad intermediate region of the phase space, with a $P_{50}(A_S)$ of 0.692. Failures on peripheral branches affect limited portions of the system, whereas the failures of structurally central connectors cause much larger connectivity losses. Meshed networks show a pronounced structural redundancy as only 59.2% of connectors are bridges, where $\mu(A_T)$, $\mu(A_L)$, $\mu(A_{LCC})$, and $P_{50}(A_S)$ are up to 0.925, 0.955, 0.973, and 0.994, respectively. The meshed pipeline systems absorb most isolated failures through alternative paths, although a small number of outlying states reveals residual topological bottlenecks.

The normalized resistance capacity R_i from the 95th percentile of failure probability is then quantified, and combined with the corresponding absorptive capacity to derive the system seismic resilience. The results are shown in **Figs. 4d, e and f**. The seismic resilience drops consistently with increased hydrogen blending ratio and exposure time, but the magnitude of loss depends strongly on pipeline topology. Relative to the baseline condition (i.e., $\alpha = 0\% \,\&\, t = 0$ yr), the linear trunklines experience the largest drop, with $\mu(SR)$ decreasing from 0.920 to 0.709 under the condition of $\alpha = 20\% \,\&\, t = 30$ yrs. The branched networks show an intermediate response, with $\mu(SR)$ decreasing from 0.948 to 0.807, equivalent to a 14.9% loss. As a comparison, the meshed networks remain comparatively resilient, with $\mu(SR)$ decreasing from 0.993 to 0.972, a loss of 2.1% only. It is thus seen that the hydrogen exposure decreases the resilience resistance on all systems, while the pipeline topology governs how the resilience degradation translates into the system-level connectivity loss. It is noted that the results describe isolated failures on pipelines. Crossings within the entire pipeline system may nevertheless share a common active fault.

Correlated systemic vulnerability under common-fault failures

The failure connectors are grouped by active faults along the route of each pipeline to identify common-fault multi-point failure scenarios (Extended Data Table 12), and 178 event sets are identified on 82 pipeline systems. Linear trunklines contain 66 event sets across 47 systems, branched networks contain 38 sets across 21 systems, and meshed networks contain 74 sets across 14 systems. More event sets in the meshed networks reflect a greater spatial extent and topological complexity, increasing the likelihood that an active fault intersects a pipeline at multiple locations.

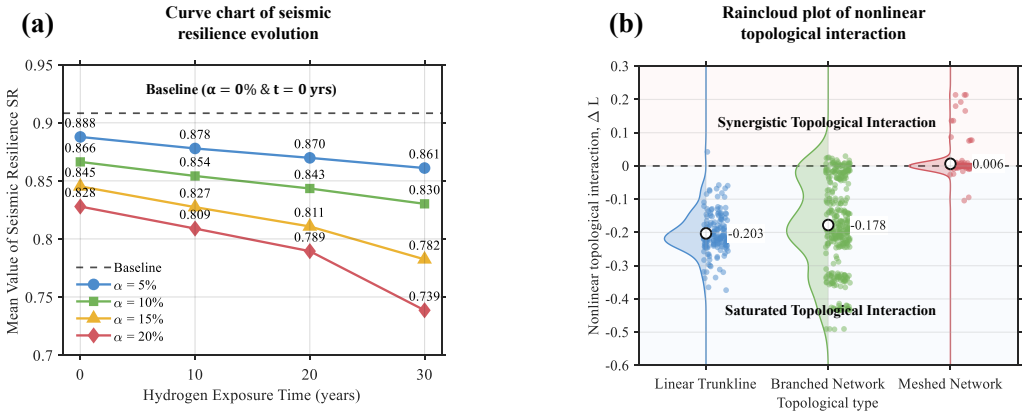


Fig. 5. Seismic resilience under common-fault multi-point failures. **a.** Chart of the seismic resilience evolution showing the mean seismic resilience of pipeline systems under common-fault multi-point failure scenarios as a function of the hydrogen exposure time. **b.** Raincloud plot of nonlinear topological interaction.

Multi-point failures on a pipeline along a common fault result in a large loss in seismic resilience of the pipeline, as compared with isolated logical-connector failures. **Fig. 5a** and Extended Data Table 13 shows the mean seismic resilience $\mu(SR_{j,f})$ of pipelines under common-fault multi-point failure scenarios as a function of the hydrogen exposure time. The results are pooled on all pipeline topologies and include only common-fault event sets involving at least two logical failure connectors. Colored lines refer to the hydrogen blending ratio (e.g., 5%, 10%, 15%, and 20%), and the horizontal dashed line denotes the base condition ($\alpha = 0\%$ and $t = 0$ yr). For 20% hydrogen-blending with 30 yrs of exposure, $\mu(SR_{j,f})$ of linear trunklines is 0.549, decreasing from 0.839 under the base condition (i.e., 34.7% loss). The branched network is associated with a

smaller decrease from 0.881 to 0.668, equivalent to 24.2% loss. However, the meshed network remains robust, with the resilience decreasing from 0.987 to 0.953, a loss of 3.5% only.

The hydrogen exposure also increases the likelihood of connector failures (Extended Data Table 14). For linear trunklines, $\mu[P(N_F \geq 2)]$ increases from the base value of 0.078 to 0.477. The probability increases from 0.164 to 0.654 and from 0.205 to 0.670 in the branched and meshed networks, respectively. Thus, hydrogen exposure increases not only the failure probability of individual points, but also the probability that multi-point failure combinations are triggered by the same fault event. Overall, common-fault events amplify the loss in seismic resilience, but the topological redundancy of pipelines buffers this effect. As a result, the meshed pipeline network remains the greatest seismic resilience even under correlated multi-point failures.

To further investigate the contribution of pipeline topology to correlated failures, the actual connectivity loss of each multi-connector joint failure is compared with the results derived from isolated connector failures, as shown in **Fig. 5b** and Extended Data Table 15. For each joint failure state, ΔL is defined as the difference between the actual connectivity loss caused by simultaneous removal of multiple logical connectors and the loss resulted from isolated connector failures. A positive ΔL indicates a synergistic topological interaction, where simultaneous failures produce a greater connectivity loss compared to isolated failures. A negative ΔL indicates saturated or overlapping interactions, where multiple failures affect overlapping network regions and produce a limited additional loss. Half-violin shapes show the distribution density, and the dashed horizontal line marks $\Delta L = 0$. Linear trunklines and branched networks are dominated by negative ΔL, with the mean values of -0.203 and -0.178, respectively. Only 0.6% of the multi-connector states in linear trunklines and 9.1% in branched networks show positive nonlinear interactions, indicating that initial failures cause most of connectivity losses. Meshed networks exhibit a distinct interaction regime, where the ΔL distribution is shifted towards zero and develops a positive tail. $\mu(\Delta L)$ becomes slightly positive (i.e., 0.006), 24.9% of joint failures show positive nonlinear interactions,

and $\max(\Delta L)$ is up to 0.214. The largest positive interactions occur in the SoCalGas system, where common-fault events associated with the Puente Hills and Elysian Park faults disrupt nominally alternative routes. Meshed networks thus remain the greatest resilience, but their redundancy is not necessarily spatially independent of common seismic disturbances.

Discussion

Hydrogen blending elevates the seismic failure risk of pipelines

This study investigates the interaction of hydrogen-induced material degradation upon exposure to high-pressure hydrogen gas with the seismic fault displacement to reshape pipeline's failure risk and resilience. The research outcome shows that the hydrogen effect persists as a latent structural vulnerability, degrading the material properties and reducing the resistance of pipelines to external geohazards such as seismic fault displacements, with pronounced nonlinear accumulation over time. As indicated in Fig. 1, nearly one-fifth of the global natural gas pipelines intersect active faults, and about two-thirds of the identified fault-crossing risk points are located in high seismic hazard regions (SHELs 4 and 5). Particularly, the seismic fault displacement has been recognized as one of the major threats to pipeline integrity. The analysis results of annualized pipeline failure probabilities in Fig. 2 show that the seismic failure risk of hydrogen-blended natural gas pipelines is governed by the interaction between external geohazards and the evolving degradation of pipe steel. The hydrogen exposure mainly increases the affected population of fault crossings, rather than worsens a small number of certain hotspots. Moreover, the greatest hydrogen-induced seismic risk effect does not necessarily coincide with the longest period of seismic hazard exposure. This non-monotonic relationship undoubtedly reshapes the global seismic risk landscape. Of particular concern, some regions with relatively low seismic hazard exposure levels, such as Australia and Germany, may experience pronounced enhancement of the seismic risk under long-term hydrogen exposure. This suggests that pipeline routing based solely on assessment of

conventional seismic geohazards may substantially underestimate the failure risk, potentially leading to catastrophic consequences.

The resulting increase in seismic failure probability becomes a system-level concern when the affected pipe segments operate in the critical sites within the pipeline topology. The difference in resilience loss on the pipelines shows that topology types determine whether the degraded structural integrity remains a local vulnerability and would propagate into a system-wide disruption. Under isolated failures, the mean retained terminal connectivity is 0.026 for linear trunklines, and 0.925 for meshed networks, showing the protection capability offered by system redundancy. The predominantly negative topological interactions in linear and branched systems indicate that joint failures often cause less connectivity loss than the isolated-failure effect (Fig. 5).

Yet system redundancy offers only conditional protection against spatially correlated seismic disturbances. Routes that are distinct in graph space may cross the same active fault and fail in a common event, simultaneously removing nominally alternative paths. Although meshed networks retain a higher mean resilience under common-fault scenarios, 24.9% of their enumerated joint-failure states exhibit positive topological interactions, with the connectivity losses exceeding those expected from isolated failures. When the hydrogen effect on degradation of pipe steel properties increases the fragility at spatially related crossings, the failure can interact through network dependency, transforming local degradation into systemic risk. Pipeline safety should, therefore, be evaluated across material, structural and system scales, while assessing the redundancy jointly in topological and geographic space.

Implications for integrity and safety maintenance of hydrogen pipelines

Existing natural gas pipelines offer essential infrastructure for large-scale hydrogen transport and deployment, avoiding initial substantial investments in constructing dedicated hydrogen pipelines. In high-pressure gaseous environments, adverse effects of hydrogen on mechanical

properties of pipe steels may occur, leading to the so-called hydrogen embrittlement such as reduced ductility and fracture toughness and increased fatigue crack propagation rate, and even cracking. The hydrogen-induced material degradation is usually a delayed process, depending on evolution of the material properties under the hydrogen effect combined with stress conditions where the pipeline experiences.

A pipeline considered suitable for hydrogen blending with certain ratios, exposure durations and seismic setting may change its condition during service. Pilot tests under specific blending limits and short-duration demonstrations cannot, on their own, establish the long-term seismic suitability across a wide variety of geohazard regions. Planning priorities should integrate four dimensions, i.e., seismic geohazard, infrastructure condition, topological criticality, and common-fault exposure. The assessment technique is shifting from identifying the aggressive geohazards to locating the time-dependent pipeline fragility that potentially produces systematic consequences. Fault crossings located at bridge connectors that control major branches, or those that expose multiple nominally alternative routes to the same active fault, should receive particular attention. Depending on the risk profile, actions may include condition-based operation, more frequent inspections, pressure reduction, targeted reinforcement, rerouting or selective replacement. Alternative paths should be credited as effective redundancy only when they are geographically independent.

Pipelines repurposing for hydrogen service should be evaluated over the full lifecycle rather than against initial capital investment alone. The benefits realized from the rapid deployment of hydrogen energy and avoided pipeline construction must be balanced against long-term requirements for integrity management and risk mitigation. Repurposing may remain a viable transition strategy in some systems, whereas others may require a strong intervention or dedicated hydrogen infrastructure to prevent evolving into long-term systemic seismic liabilities.

Methods

Data sources

We compiled a global inventory of operating natural gas pipelines from the Global Gas Infrastructure Tracker (GGIT) maintained by Global Energy Monitor. The resulting inventory comprised 2,554 operating natural gas pipelines with a combined reported length of approximately 1.11 million km. The database provided spatially explicit pipeline routes and associated attributes, including pipeline and segment names, countries or areas traversed, commissioning year, transport capacity, diameter and reported length. This inventory provided the common infrastructure basis for subsequent analyses of seismic hazard exposure, failure probability and network resilience.

Seismic ground-motion hazard was characterized using the Global Earthquake Model (GEM) Global Seismic Hazard Map (Version 2023), which provides peak ground acceleration (PGA) under reference rock site conditions for a 10% probability of exceedance in 50 years at a spatial resolution of 3 arc-min. Active fault geometries were obtained from the GEM Global Active Faults Database. The processed dataset comprised 13,696 mapped fault traces with associated information on fault identity, slip type, activity class and positional accuracy, and was used to identify intersections between operating natural gas pipelines and mapped active faults. All vector datasets were harmonized to the World Geodetic System 1984 coordinate reference system, and features with missing, empty or unusable geometries were excluded before analysis.

Seismic hazard exposure of pipelines

We sampled PGA values along each pipeline geometry at approximately 10 km intervals. Each pipeline was treated as a complete linear object, with all constituent line segments indexed by cumulative geodesic length before sampling. This approach ensured a consistent sampling density along the entire pipeline and avoided the disproportionate representation of pipelines stored as multiple geometry segments. Sampling included the pipeline endpoints, whereas pipelines shorter

than 10 km were represented by a single sample at their midpoint. PGA values were extracted from the raster cell containing each sampling location. No-data values, non-finite values, negative values and values exceeding 10 g were excluded. The 95th percentile of the sampled PGA distribution was used as the pipeline-level seismic exposure metric, as $P_{95}(\mathrm{PGA})$ captures relatively high seismic exposure along a pipeline while reducing sensitivity to isolated raster extremes. Five seismic hazard exposure levels (SHELs) are defined based on $P_{95}(\mathrm{PGA})$, i.e., SHEL 1 $\in$ [0 g, 0.05 g); SHEL 2 $\in$ [0.05 g, 0.10 g); SHEL 3 $\in$ [0.10 g, 0.20 g); SHEL 4 $\in$ [0.20 g, 0.40 g); SHEL 5 $\geq$ 0.40 g.

Identification of fault-crossing risk points

We identified potential fault-crossing risk points by calculating the exact geometric intersections between operating natural gas pipeline routes and mapped active fault traces. A spatial index was first used to screen fault traces whose spatial extents overlapped each pipeline, after which exact line intersections were calculated for each candidate pipeline-fault pair. Single-point intersections were retained directly, whereas multipoint intersections were separated into individual crossing candidates. Where a pipeline and fault overlapped along a line segment, the overlapping segment was represented by a single interior point.

The continuous PGA raster was sampled at each candidate fault-crossing risk point to characterize the local seismic hazard. Each point was subsequently assigned to one of the five seismic hazard exposure levels using the PGA thresholds defined above. Candidate points without valid raster values were retained as No Data. To avoid repeated counting arising from fragmented or closely spaced geometries, candidate points associated with the same pipeline-fault pair were deduplicated using a 5 km distance threshold. A seed-based clustering procedure was applied after projecting the points to a metric coordinate system, and one representative point was retained from each cluster. Where multiple candidates occurred within the same cluster, preference was given to the point with the highest valid local PGA. After excluding 14 risk points without valid PGA values,

1,731 risk points were retained for the subsequent seismic failure probability analysis.

Calculation of seismic failure probability

For pipelines crossing active faults, the annualized pipeline failure probabilities $P_{an,f}$ caused by potential seismic fault displacement were calculated.

$$P_{an,f} = \lambda_{eq} P(F|X) \quad (1)$$

$$\lambda_{eq} = -\frac{\ln(1-0.1)}{50} = 2.107 \times 10^{-3}\ \mathrm{yrs}^{-1} \quad (2)$$

where λ_{eq} denotes the equivalent annual seismic occurrence rate derived from the GEM Global Seismic Hazard Map (version 2023.1), assuming a stationary Poisson process [33]. $P(F|X)$ is the conditional failure probability given the system state vector $X = [D, t_r, P, a, d, \theta, \alpha, t]$. D is the pipeline diameter, [mm]; t_r is the remaining shell thickness, [mm]; P is the operating pressure, [MPa]; a is the fatigue crack size, [mm]; d is the fault displacement, [mm]; θ is the fault crossing angle, [rad]; α is the hydrogen blending ratio, [%]; t is the hydrogen exposure time, [yrs].

In this study, we applied the seismic fragility model developed in our previous work to estimate $P(F|X)$ for hydrogen-blended natural gas pipelines. The model captures the time-dependent evolution of failure probability under seismic loading by explicitly linking macroscopic fragility to the nonlinear degradation of pipeline steel, including hydrogen-assisted crack propagation, reduction in fracture toughness, and corrosion-driven defect growth under high-pressure hydrogen exposure.

For each fault-crossing risk point, the corresponding system state vectors were constructed to be the input of seismic fragility model. The pipeline diameter D is the fixed parameter extracted from the GGIT dataset. θ is another fixed parameter that can be determined by the fault type [34, 35].

$$\theta = \begin{cases} \frac{\pi}{2} - \theta_{pfc}, \text{Strike} - \text{slip faults} \\ \frac{\pi}{6}, \text{normal faults} \\ \frac{\pi}{3}, \text{reverse faults} \\ \frac{\pi}{4}, \text{others} \end{cases} \quad (3)$$

where θ_{pfc} is the pipeline-fault crossing angle, [rad]. The operating pressure $P \sim U(6, 20)$ was treated as a stochastic parameter to represent global variability in pipeline operating conditions. Considering the diversity of transmission systems and design standards across countries, P was assumed to follow a uniform distribution within a physically representative range of [6 MPa, 20 MPa]. Fault displacement d was represented stochastically using the all-slip-type magnitude–average surface displacement relationship developed by Wells and Coppersmith [36].

$$\log_{10}(d) = -1.80 + 0.69M + \varepsilon \quad (4)$$

where M is moment magnitude, which can be assigned based on PGA-conditioned seismic intensity classes; $\varepsilon \sim N(0, 0.36)$ represents the residual variability in the empirical magnitude–displacement relationship. Because the original relationship characterizes displacement averaged along the surface rupture, the resulting d was treated as a stochastic proxy for the fault displacement imposed at each risk points.

The hydrogen blending ratio α and hydrogen exposure time t are defined as deterministic scenario parameters representing engineered hydrogen transition conditions. The hydrogen blending ratio was specified at four levels (5%, 10%, 15%, and 20%), and the hydrogen exposure time was defined at three levels (10, 20, and 30 years), representing progressively increasing hydrogen integration and operational exposure scenarios in pipeline systems. The remaining shell thickness t_r and fatigue crack size a are treated as two hydrogen-blending-controlled structural degradation parameters. A semi-empirical model [37] provided by Sandia National Laboratories was adopted to model the fatigue crack growth behavior $a(t)$ under hydrogen-containing conditions.

$$\frac{da}{dt} = (8.83 \times 10^{-6}) f \left(\frac{1 + 0.4286R}{1 - R}\right) (\Delta K)^{6.5} \sqrt{f_{H_2}} \quad (5)$$

where $\frac{da}{dt}$ is the crack growth rate $[mm \cdot yrs^{-1}]$; f is the cyclic loading frequency, [Hz]; R is the stress ratio; f_{H_2} is the hydrogen fugacity, [MPa]; ΔK is the stress intensity factor range, $[MPa \cdot \sqrt{m}]$.

Hydrogen destabilizes the passive film and enhances electrochemical activity, thereby accelerating corrosion and promoting the initiation and growth of corrosion defects [38, 39]. Accordingly, corrosion depth is modeled as a time-dependent function that explicitly accounts for the effects of hydrogen exposure [40, 41].

$$t_r(t) = t_s - c_d(t) \quad (6)$$

$$c_d(t) = k_0 t^n \left(1 + \varphi \sqrt{f_{H_2}}\right) \quad (7)$$

$$\varphi = \begin{cases} 0.750, \alpha \in (0, 0.1] \\ 1.500, \alpha \in (0.1, 0.3] \\ 2.500, \alpha \in (0.3, 1] \end{cases} \quad (8)$$

where t_s is the design shell thickness of pipelines, [mm]; $c_d(t)$ is the time-dependent corrosion depth, [mm]; k_0 is the corrosion rate under hydrogen-free conditions, $[mm \cdot yrs^n]$; n is the time exponent; φ is the hydrogen effect coefficient, which is defined as a piecewise function of hydrogen blending ratio.

A Monte Carlo simulation framework is implemented to propagate uncertainty in seismic demand (fault displacement), operating conditions (operating pressure), and hydrogen-induced degradation processes (initial crack size and design shell thickness). To determine an appropriate Monte Carlo sample size, a convergence analysis was conducted using sample sizes ranging from N = 50 to N = 1000. The convergence behavior was evaluated in terms of the mean, median, and 95th percentile of the conditional failure probability, as well as the proportion of truncated samples. The results (Extended Data Table 16) indicate that the mean and median values converge rapidly

even at small sample sizes, whereas the upper-tail statistic $P_{95}(P(F|X))$ exhibits slower convergence. When N = 500, the relative deviation of $P_{95}(P(F|X))$ from the reference case (N = 1000) is reduced to 0.44%, indicating that the tail distribution has effectively stabilized. Thus, in this study, N = 500 is adopted as the baseline Monte Carlo sample size, providing a balance between computational efficiency and statistical convergence, particularly for upper-tail risk estimation.

Pipeline system topology

On the basis of GGIT data, multipart pipeline features were first decomposed into individual line segments and projected to a regional planar coordinate system [42,43,44]. Considering the coordinate deviation of risk points, each of them was projected to the nearest position on its corresponding pipeline geometry. Risk points projected to the same segment within 1 m were consolidated as a common topological failure location. For each pipeline system j, the baseline topology was represented as a weighted undirected multigraph G_j^0[45].

$$G_j^0 = \left(V_j, E_j^{phy} \cup E_j^{risk}\right) \tag{9}$$

where V_j denotes the node set, including pipeline terminals, junctions and intermediate segmentation points; E_j^{phy} comprises physical pipeline edges weighted by their lengths; E_j^{risk} comprises zero-length logical failure connectors introduced at fault-crossing risk points. Pipeline terminals were defined as degree-one physical nodes in the baseline topology, excluding the auxiliary nodes associated with logical failure connectors. According to the structural complexity of pipeline system, three general topological types were defined.

$$\begin{cases} n_j^T = 2 \ \wedge \ \mu_j = 0, \text{Linear Trunkline} \\ n_j^T > 2 \ \wedge \ \mu_j = 0, \text{Branched Network} \\ \mu_j > 0, \text{Meshed Network} \end{cases} \tag{10}$$

$$\mu_j = | E_j | - | V_j | + N_{c,j} \tag{11}$$

where n_j^T is the number of baseline terminal nodes in pipeline system j; μ_j represents the number

of independent cycles in the network; $|E_j|$ is the total number of edges in the baseline graph, including physical edges and logical failure connectors; $|V_j|$ is the total number of nodes; $N_{c,j}$ is the number of connected components. $\mu_j = 0$ indicates an acyclic structure, whereas $\mu_j > 0$ indicates the presence of one or more alternative paths.

Seismic resilience under isolated logical-connector failures

The seismic failure of pipeline at fault-crossing risk point i can be regarded as the elimination of corresponding logical failure connector.

$$G_{j,i}^{-} = G_j^0 - e_i^{risk} \tag{12}$$

where e_i^{risk} is the logical failure connector associated with fault-crossing risk point i; $G_{j,i}^{-}$ is the seismic damaged topology. A logical connector was identified as a bridge failure location when its removal increased the number of connected components.

$$B_{j,i} = \begin{cases} 1, N_c(G_{j,i}^{-}) > N_c(G_j^0) \\ 0, \text{otherwise} \end{cases} \tag{13}$$

where $B_{j,i}$ is the bridge indicator; $N_c(G)$ is the number of connected components in graph G. A value of $B_{j,i} = 1$ indicates that seismic failure of pipeline at fault-crossing risk point i divides at least one previously connected part of the pipeline system j, whereas $B_{j,i} = 0$ indicates that alternative paths preserve network connectivity.

In this study, seismic resilience is defined as the capacity of a pipeline system to maintain functional and physical connectivity under seismic disturbance through two key components, resistance and absorptive capacity [24,46-48].

(1) System resistance capacity

System resistance capacity describes the ability of fault-crossing pipelines to withstand seismic loading without failure. A normalized system resistance capacity metric R_i is defined on the basis of conditional failure probability.

$$R_i = 1 - P(F|X_i) \tag{14}$$

where $P(F|X_i)$ denotes the conditional failure probability given the system state vector of fault-crossing risk point i. The value of R_i ranges from 0 to 1, with higher values indicating a greater capacity to remain operational under seismic disturbance.

(2) System absorptive capacity

System absorptive capacity was defined as the ability of a pipeline topology to retain connectivity after the failure of fault-crossing risk points [49,50]. In this study, the retained terminal-to-terminal connectivity A_T, retained length-weighted network integrity A_L and retained largest-component size A_{LCC} were adopted to characterize system absorptive capacity from three complementary perspectives.

$$A_{T,j,i} = \frac{\sum_{(a,b)\in\mathcal{P}_j^0} w_{ab}\, I(a \leftrightarrow b|G_{j,i}^-)}{\sum_{(a,b)\in\mathcal{P}_j^0} w_{ab}} \tag{15}$$

$$\mathcal{P}_j^0 = \{(a,b): a,b \in T_j, a \leftrightarrow b \text{ in } G_j^0\} \tag{16}$$

where $A_{T,j,i} \in [0,1]$ is the retained terminal-connectivity capacity following the seismic failure of pipeline at fault-crossing risk point i; a and b are baseline terminal nodes; w_{ab} is the weight assigned to terminal pair (a,b); $I(\cdot)$ is an indicator function equal to 1 when terminals a and b remain connected and 0 otherwise; T_j denote the set of physical terminal nodes in the baseline topology; $\mathcal{P}_j^0$ denote the set of terminal pairs connected under the baseline condition. Because pipeline-specific supply, demand and flow data were unavailable, all terminal pairs were assigned equal weights $w_{ab} = 1$. $A_{T,j,i} = 1$ indicates that all baseline terminal pairs remain connected, whereas a value of 0 indicates that none of the baseline terminal pairs remain connected. For a two-terminal linear trunkline, $\mathcal{P}_j^0$ contains only one terminal pair, and $A_{T,j,i}$ therefore reduces to a binary measure of end-to-end continuity. For branched networks, $A_{T,j,i} \in [0,1]$ represents the proportion of terminal pairs that remain mutually connected. For meshed networks, $A_{T,j,i}$ captures

the ability of alternative paths to preserve terminal connectivity following the removal of a local connector.

Furthermore, retained length-weighted network integrity $A_{L,j,i}$ was calculated.

$$A_{L,j,i} = \frac{Q_L(G_{j,i}^-)}{Q_L(G_j^0)} \tag{17}$$

$$Q_L(G) = \sum_{c=1}^{N_c(G)} \left(\frac{L_c}{L_{tot}}\right)^2 \tag{18}$$

where $Q_L(G)$ is the length-weighted network integrity; L_c is the total length of physical pipeline edges contained in connected component c, [km]; L_{tot} is the total physical length of the pipeline system, [km]; $N_c(G)$ is the number of connected components. $A_{L,j,i}$ represents the proportion of baseline length-weighted network integrity retained after the seismic failure of pipeline at fault-crossing risk point i. Values approaching 1 indicate limited structural fragmentation, whereas lower values indicate that the physical pipeline length has been divided among multiple disconnected components.

Ultimately, retained largest-component size $A_{LCC,j,i}$ was calculated.

$$A_{LCC,j,i} = \frac{L_{max}(G_{j,i}^-)}{L_{max}(G_j^0)} \tag{19}$$

where $L_{max}(G)$ is the total physical pipeline length contained in the largest connected component of graph G. This metric measures the proportion of the largest continuous pipeline section retained immediately after seismic failure of pipeline at fault-crossing risk point i.

We therefore defined a composite normalized system absorptive capacity metric by equally weighting the three complementary dimensions of retained system connectivity.

$$A_{S,j,i} = \frac{A_{T,j,i} + A_{L,j,i} + A_{LCC,j,i}}{3} \tag{20}$$

where $A_{S,j,i}$ ranges from 0 to 1, with larger values indicating a greater capacity of pipeline system j to absorb the isolated failure of logical connector i while retaining system connectivity.

(3) Seismic resilience

For fault-crossing risk point i in pipeline system j, the corresponding logical connector remains operational with probability R_i, in which case the baseline system connectivity is fully retained. If the connector fails with probability $1 - R_i$, the pipeline system retains a fraction $A_{S,j,i}$ of its baseline connectivity. A normalized seismic resilience metric $SR_{j,i}$ was therefore defined as the expected proportion of system connectivity retained under seismic disturbance.

$$SR_{j,i} = R_i + (1 - R_i)A_{S,j,i} \tag{21}$$

where $SR_{j,i} \in [0,1]$ denotes the seismic resilience of pipeline system j associated with fault-crossing risk point i. Larger values indicate a greater capacity to maintain connectivity under seismic disturbance. A value of 1 indicates that system connectivity is fully retained, either because the connector remains operational or because its failure is completely absorbed by the network topology. A value of 0 indicates certain connector failure accompanied by complete loss of system connectivity.

Seismic resilience under common-fault multi-point failures

Given that seismic fault displacement may trigger multi-point failures, we extended the isolated logical-connector framework to evaluate pipeline-system resilience under common-fault multi-point failure scenarios. Fault-crossing risk points associated with the same active fault within a pipeline system were grouped as a co-occurring event set $\mathcal{I}_{j,f}$.

$$\mathcal{I}_{j,f} = \{i \in pip_j | fault(i) = f\} \tag{22}$$

where pip_j denotes all fault-crossing risk points in pipeline system j; $fault(i)$ denotes the fault associated with risk point i. For a co-occurring event set, a joint failure state was represented by a subset.

$$\mathcal{S} \subseteq \mathcal{I}_{j,f} \tag{23}$$

$$\pi_{j,f,\mathcal{S}} = \prod_{i \in \mathcal{S}} P(F|X_i) \prod_{k \in \mathcal{J}_{j,f} \wedge k \notin \mathcal{S}} [1 - P(F|X_i)] \tag{24}$$

where the risk points contained in $\mathcal{S}$ fail and the remaining risk points remain operational; $\pi_{j,f,\mathcal{S}}$ denotes joint failure probability of $\mathcal{S}$. The corresponding damaged topology was obtained by simultaneously removing all logical failure connectors associated with $\mathcal{S}$.

$$G^{-}_{j,f,\mathcal{S}} = G^{0}_{j} - \left\{ e^{risk}_{i} | i \in \mathcal{S} \right\} \tag{25}$$

The retained terminal-to-terminal connectivity $A_{T,j,f,\mathcal{S}}$, retained length-weighted network integrity $A_{L,j,f,\mathcal{S}}$, and retained largest-component size $A_{LCC,j,f,\mathcal{S}}$ were recalculated on $G^{-}_{j,f,\mathcal{S}}$ using the definitions introduced for isolated connector failures. The absorptive capacity associated with $\mathcal{S}$ was then defined as follows.

$$A_{S,j,f,\mathcal{S}} = \frac{A_{T,j,f,\mathcal{S}} + A_{L,j,f,\mathcal{S}} + A_{LCC,j,f,\mathcal{S}}}{3} \tag{26}$$

The seismic resilience of pipeline system j conditional on common fault event f was defined as the expected proportion of system connectivity retained across all possible $\mathcal{S}$.

$$SR_{j,f} = \sum_{\mathcal{S} \subseteq \mathcal{J}_{j,f}} \pi_{j,f,\mathcal{S}} A_{S,j,f,\mathcal{S}} \tag{27}$$

Limitations and scope of inference

Several limitations define the scope of our methods. The GGIT provides a globally consistent infrastructure inventory, but lacks harmonized information on steel grade, wall thickness, weld quality, pre-existing defects, operating pressure and maintenance history. Pipeline routes and active-fault geometries also vary in spatial accuracy and level of generalization. The identified fault crossings should therefore be interpreted as globally consistent exposure-screening locations rather than engineering-grade representations of individual pipeline-fault intersections. Moreover, a mapped crossing indicates potential exposure to surface rupture, not that the associated fault will necessarily rupture during the assessment period.

The annualization framework also involves simplifying assumptions. The equivalent

occurrence rate assumes a stationary Poisson process and does not represent fault-specific recurrence intervals, slip rates, event clustering or local site conditions. Conditioning earthquake magnitude on PGA and estimating displacement from empirical scaling relationships cannot fully capture rupture length, spatial slip variability or near-fault effects. Hydrogen-induced degradation is likewise represented through semi-empirical relationships and scenario parameters, and cannot replace pipeline-specific material testing and integrity assessment. In common-fault scenarios, equation (24) constructs joint states by multiplying point-level failure probabilities conditional on the shared event, thereby assuming conditional independence and omitting spatial dependence in seismic demand, soil response and pipeline condition. The resulting annualized probabilities should therefore be treated as globally harmonized screening metrics rather than site-specific engineering predictions.

Finally, the resilience metric captures resistance and immediate topology-based connectivity retention, but not hydraulic flow, supply-demand weighting, operational control, repair time or service losses. It therefore represents immediate connectivity-based seismic resilience rather than full post-earthquake service recovery. Systemic seismic risk is therefore interpreted here as network-wide connectivity disruption arising from dependent component failures. Within these boundaries, we provide a globally harmonized basis for identifying transition-sensitive risk patterns and prioritizing pipeline systems for detailed investigation.

Acknowledgements

This study was supported by the National Natural Science Foundation of China (Grant No. 52402421 and W2531036), Ningbo Yongjiang Talent Programme (Grant No. 2025D-136-05), the Postdoctoral Science Foundation of Zhejiang Province (Grant No. ZJ2026114), and Open Fund (OGE202501-04) of Key Laboratory of Oil & Gas Equipment, Ministry of Education (Southwest Petroleum University).

Author contribution declaration

Jinkun Men, the first author: Research data for the article, research idea and planning, substantial contribution to the discussion of content, and writing of the original manuscript. Hongfang Lu: Research data for the article, and participation in discussion of the research content. Yinghao Sun: Research data for the article. Jie Zhang: Research data for the article, and project coordination. Y. Frank Cheng, the corresponding author: research idea and planning, substantial contribution to the discussion of content, supervision, and review/editing of manuscript before submission.

Competing interests

The authors declare no competing interests.

Data availability

We use publicly available data from the Global Gas Infrastructure Tracker (GGIT), maintained by Global Energy Monitor, for the locations, routes and attributes of operating natural gas pipelines (available at https://globalenergymonitor.org/research/explore-global-gas-infrastructure-tracker-gas-pipelines-dashboard); the Global Earthquake Model (GEM) Global Seismic Hazard Map (version 2023.1) for global peak ground acceleration (available at https://www.globalquakemodel.org/product/global-seismic-hazard-map); and the GEM Global Active Faults Database for active fault geometries and associated attributes (available at https://www.globalquakemodel.org/product/active-faults-database).

References

1. Ouyang, Z.*, et al.* The global hydrogen budget. *Nature* **648**, 616-624 https://doi.org/10.1038/s41586-025-09806-1 (2025).
2. van Renssen, S. The hydrogen solution? *Nature Climate Change* **10**, 799-801 https://doi.org/10.1038/s41558-020-0891-0 (2020).
3. Löfving, J., Brynolf, S., Grahn, M., Öberg, S. & Taljegard, M. Resource requirements and consequences of large-scale hydrogen use in Europe. *Nature Sustainability* **9**, 614-625 https://doi.org/10.1038/s41893-026-01771-5 (2026).
4. Satyapal, S. The highs and lows of hydrogen. *Nature Energy* **11**, 12-13 https://doi.org/10.1038/s41560-025-01917-3 (2026).
5. Terlouw, T.*, et al.* Global greenhouse gas emissions mitigation potential of existing and planned hydrogen projects. *Nature Energy* **10**, 1503-1515 https://doi.org/10.1038/s41560-025-01892-9 (2025).
6. Hauglustaine, D.*, et al.* Climate benefit of a future hydrogen economy. *Communications Earth & Environment* **3**, 295 https://doi.org/10.1038/s43247-022-00626-z (2022).
7. Terlouw, T., Rosa, L., Bauer, C. & McKenna, R. Future hydrogen economies imply environmental trade-offs and a supply-demand mismatch. *Nature Communications* **15**, 7043 https://doi.org/10.1038/s41467-024-51251-7 (2024).
8. Konovalov, D. & Adams, T. A. Hydrogen power development: A comparative review of national strategies and the role of energy in scaling green hydrogen. *Renewable and Sustainable Energy Reviews* **226**, 116378 https://doi.org/10.1016/j.rser.2025.116378 (2026).
9. Hofmann, F., Tries, C., Neumann, F., Zeyen, E. & Brown, T. H_2 and CO_2 network strategies for the European energy system. *Nature Energy* **10**, 715-724 https://doi.org/10.1038/s41560-025-01752-6 (2025).
10. Gül, T., Remme, U., Menendez, J. M. B., Blanco, H. & Pizarro, A. Global Hydrogen Review 2026.). International Energy Agency (2026).
11. Men, J., Lu, H. & Cheng, Y. F. Energy pipeline engineering towards carbon neutrality target: States-of-the-art, safety challenges, and mode-shifting. *Journal of Traffic and Transportation Engineering*, 1-33 https://doi.org/10.19818/j.cnki.1671-1637.2026.242 (2026).
12. Johnson, N.*, et al.* Realistic roles for hydrogen in the future energy transition. *Nature Reviews Clean Technology* **1**, 351-371 https://doi.org/10.1038/s44359-025-00050-4 (2025).
13. Zhou, L.*, et al.* Hydrogen blending into natural gas networks: global practices, infrastructure compatibility, and end-user implications. *Applied Energy* **402**, 127057 https://doi.org/10.1016/j.apenergy.2025.127057 (2026).
14. Lu, H. Urban gas infrastructure meets hydrogen ambitions. *Nature Cities* **2**, 773-774 https://doi.org/10.1038/s44284-025-00308-9 (2025).
15. Department for Energy Security and Net Zero. Hydrogen Blending into GB Gas Distribution Networks: A Strategic Policy Decision.) (2023).
16. Isaac, T. HyDeploy: The UK's First Hydrogen Blending Deployment Project. *Clean Energy* **3**, 114-125 https://doi.org/10.1093/ce/zkz006 (2019).
17. Pang, L.*, et al.* Explosion venting of indoor hydrogen-blended natural gas: Distribution law

of compound hazards driven by "leakage-accumulation" effect. *International Journal of Hydrogen Energy* **101**, 379-390 https://doi.org/10.1016/j.ijhydene.2024.12.460 (2025).
18. Brissaud, F., Chaise, A., Gault, K. & Soual, S. Lessons learned from Jupiter 1000, an industrial demonstrator of Power-to-Gas. *International Journal of Hydrogen Energy* **49**, 925-932 https://doi.org/10.1016/j.ijhydene.2023.10.003 (2024).
19. Xing, X.*, et al.* Effects of alloy elements on the hydrogen adsorption behavior of pipeline steel: A review. *Renewable and Sustainable Energy Reviews* **222**, 116003 https://doi.org/10.1016/j.rser.2025.116003 (2025).
20. Yu, H.*, et al.* Hydrogen Embrittlement as a Conspicuous Material Challenge─Comprehensive Review and Future Directions. *Chemical Reviews* **124**, 6271-6392 https://doi.org/10.1021/acs.chemrev.3c00624 (2024).
21. Islam, A., Yoo, Y. & Girard, F. Evaluating the safety and performance of hydrogen-natural gas blends in residential and commercial appliances – testing outcomes and gap analysis. *International Journal of Hydrogen Energy* **147**, 149876 https://doi.org/10.1016/j.ijhydene.2025.06.066 (2025).
22. Groth, K. M., Li, R., Al-Douri, A., Ustolin, F. & Yang, R. Hydrogen safety for production, infrastructures, vehicles and aviation. *Nature Reviews Clean Technology*, https://doi.org/10.1038/s44359-026-00175-0 (2026).
23. Shehata, M. F. & El-Shamy, A. M. Hydrogen-based failure in oil and gas pipelines a review. *Gas Science and Engineering* **115**, 204994 https://doi.org/10.1016/j.jgsce.2023.204994 (2023).
24. Men, J., Lu, H. & Cheng, Y. F. Continuous time-dependent system resilience evolution behaviors of hazardous energy systems subjected to cascading disaster chains. *Reliability Engineering & System Safety* **267**, 111918 https://doi.org/10.1016/j.ress.2025.111918 (2026).
25. Sun, M.-m.*, et al.* Limit state equation and failure pressure prediction model of pipeline with complex loading. *Nature Communications* **15**, 4473 https://doi.org/10.1038/s41467-024-48688-1 (2024).
26. Hmaimid, Z.*, et al.* A comprehensive review on the compatibility of polymeric materials for hydrogen transportation and storage. *International Journal of Hydrogen Energy* **192**, 152366 https://doi.org/10.1016/j.ijhydene.2025.152366 (2025).
27. Islam, A.*, et al.* Hydrogen blending in natural gas pipelines: A comprehensive review of material compatibility and safety considerations. *International Journal of Hydrogen Energy* **93**, 1429-1461 https://doi.org/10.1016/j.ijhydene.2024.10.384 (2024).
28. Luo, Y.*, et al.* Large-scale shaking table tests on seismic mitigation effect of a novel flexible joint and buffer layer on TBM pipeline tunnels. *Underground Space* **28**, 451-475 https://doi.org/10.1016/j.undsp.2026.02.001 (2026).
29. Alavi, S. H. & Mashayekhi, M. Development of a seismic life cycle cost framework for buried pipelines. *Reliability Engineering & System Safety* **267**, 111874 https://doi.org/10.1016/j.ress.2025.111874 (2026).
30. Shi, H., Tan, X., He, J., Jiang, M. & Chen, C. Seismic resilience assessment of natural gas pipeline networks: an agent-based stochastic simulation approach. *Journal of Loss*

Prevention in the Process Industries **101**, 105934 https://doi.org/10.1016/j.jlp.2026.105934 (2026).
31. Huang, Y., Yang, J., Qi, S., Ma, B. & Sun, L. Resilience enhancement of island integrated energy systems under seismic hazards: A two-stage restoration strategy. *Energy* **358**, 141317 https://doi.org/10.1016/j.energy.2026.141317 (2026).
32. Pagani, M.*, et al.* OpenQuake Engine: An Open Hazard (and Risk) Software for the Global Earthquake Model. *Seismological Research Letters* **85**, 692-702 https://doi.org/10.1785/0220130087 (2014).
33. Kwong, N. S.*, et al.* Earthquake Risk of Gas Pipelines in the Conterminous United States and Its Sources of Uncertainty. *ASCE-ASME Journal of Risk and Uncertainty in Engineering Systems, Part A: Civil Engineering* **8**, 04021081 https://doi.org/10.1061/AJRUA6.0001202 (2022).
34. Karamitros, D. K., Bouckovalas, G. D. & Kouretzis, G. P. Stress analysis of buried steel pipelines at strike-slip fault crossings. *Soil Dynamics and Earthquake Engineering* **27**, 200-211 https://doi.org/10.1016/j.soildyn.2006.08.001 (2007).
35. O'Rourke, T. D., Jung, J. K. & Argyrou, C. Underground pipeline response to earthquake-induced ground deformation. *Soil Dynamics and Earthquake Engineering* **91**, 272-283 https://doi.org/10.1016/j.soildyn.2016.09.008 (2016).
36. Wells, D. L. & Coppersmith, K. J. New empirical relationships among magnitude, rupture length, rupture width, rupture area, and surface displacement. *Bulletin of the Seismological Society of America* **84**, 974–1002 https://doi.org/10.1785/BSSA0840040974 (1994).
37. Salilkumar, A. N. Fracture Toughness and Fatigue Crack Growth Rate Modelling in blended Hydrogen and Natural Gas steel pipelines.). University of California (2025).
38. Yue, X.*, et al.* Effect of hydrogen on the passivation for ultra-thin 316 L SS foil. *npj Materials Degradation* **7**, 79 https://doi.org/10.1038/s41529-023-00398-7 (2023).
39. Örnek, C.*, et al.* Understanding passive film degradation and its effect on hydrogen embrittlement of super duplex stainless steel – Synchrotron X-ray and electrochemical measurements combined with CalPhaD and ab-initio computational studies. *Applied Surface Science* **628**, 157364 https://doi.org/10.1016/j.apsusc.2023.157364 (2023).
40. Hou, Y.*, et al.* Effects of hydrogen charging on the corrosion behavior and hydrogen embrittlement of 7xxx Al Alloys: An integrated experimental and multiscale simulation study. *Corrosion Science* **257**, 113291 https://doi.org/10.1016/j.corsci.2025.113291 (2025).
41. Hredil, M., Tsyrulnyk, O., Shtoyko, I. & Zvirko, O. Influence of gaseous hydrogen on corrosion of pipeline steel. *Procedia Structural Integrity* **59**, 151-157 https://doi.org/10.1016/j.prostr.2024.04.023 (2024).
42. Liu, X., Hu, J., Wang, Y., Liu, Y.-Y. & Zhang, H.-T. Optimal dismantling of directed networks. *Nature Communications*, https://doi.org/10.1038/s41467-026-74467-1 (2026).
43. Romeijnders, M.*, et al.* Event-based spatiotemporal networks for modelling emergent phenomena in complex systems. *Nature Communications*, https://doi.org/10.1038/s41467-026-73917-0 (2026).
44. Wang, M., Ma, Z., Mehana, M. & Chen, B. SimH2: an integrated techno-economic modeling framework for hydrogen pipeline infrastructure and network optimization.

Energy Conversion and Management **366**, 121855 https://doi.org/10.1016/j.enconman.2026.121855 (2026).

45. Men, J., Chen, G., Zhou, L. & Chen, P. A pareto-based multi-objective network design approach for mitigating the risk of hazardous materials transportation. *Process Safety and Environmental Protection* **161**, 860-875 https://doi.org/https://doi.org/10.1016/j.psep.2022.03.048 (2022).
46. Logan, T. M., Aven, T., Guikema, S. D. & Flage, R. Risk science offers an integrated approach to resilience. *Nature Sustainability* **5**, 741-748 https://doi.org/10.1038/s41893-022-00893-w (2022).
47. Zheng, D.*, et al.* Strategies for climate-resilient global wind and solar power systems. *Nature* **643**, 1263-1270 https://doi.org/10.1038/s41586-025-09266-7 (2025).
48. How coastal resilience emerges. *Nature Communications* **17**, 9059 https://doi.org/10.1038/s41467-026-76127-w (2026).
49. Gao, J., Barzel, B. & Barabási, A.-L. Universal resilience patterns in complex networks. *Nature* **530**, 307-312 https://doi.org/10.1038/nature16948 (2016).
50. Artime, O.*, et al.* Robustness and resilience of complex networks. *Nature Reviews Physics* **6**, 114-131 https://doi.org/10.1038/s42254-023-00676-y (2024).

Supplementary Files

This is a list of supplementary files associated with this preprint. Click to download.

- Supplymentarydata.docx